A 3D pseudospectral method for order reduced SH wave simulation

Junxiao Li, Kristopher A. Innanen, Guo Tao and Laurence Lines

ABSTRACT

In this paper, the order reduced velocity-displacement SH-wave equations in VTI media are first proposed. During SH-wave simulation, the spatial derivatives of the new SH-wave equations are transformed into wavenumber domain and a staggered-grid Fourier pseudospectral time-domain (PSTD) method is used to obtain discretized forms of these wavenumber operators, which in turn, effectively eliminates the Gibbs phenomenon that arises when Fourier transforming a discontinuous function in heterogeneous media. The order reduced velocity-displacement SH-wave equations also make it possible to set hybrid perfectly matched layers around computational boundaries to mitigate artificial reflections. Finally, this new scheme is applied for wavefield modeling in two-layer heterogeneous media. Comparisons of simulation results with PSTD using second-order SH-wave equation further verify its accuracy.

INTRODUCTION

The most popular numerical approach used to model the propagation of seismic waves is probably the finite-difference (FD) method (Alterman and Karal, 1968; Alford et al., 1974; Kelly and Iversen, 1976; Madariaga, 1976; Virieux, 1986). SH-wave modeling using FD starts as early as Boore (1970a) applied it to SH-wave propagation in laterally inhomogeneous media. This FD representation, however, does not satisfy the equations of motion (Boore, 1970b). Kummer and Behle (1982) proposed a second-order finite-difference modeling of SH-wave propagation in laterally inhomogeneous media. Virieux (1984) rearranged the second-order hyperbolic SH-wave equation into a first-order velocity-stress hyperbolic system in a generaly heterogeneous medium. Nevertheless, he pointed out a corner wave as sell as a head wave would appear, which could pose severe problems of interpretation with migration methods. Moczo (1989) developed an explicit finite-difference scheme using irregular rectangular grids for SH-waves in 2D media, which allows the reduction of staircase diffractions and the number of grid points. Igel and Weber (1995) implemented an axisymmetric wave propagation for SH-waves in spherical coordinates with a FD technique to calculate seismograms for global earth models. Slawinski and Krebes (2002) used the homogeneous approach to derive a finite difference scheme for modeling SH-wave propagation in fractured media. Fractures were modeled as internal interfaces in nonwelded contact. The complexity and high computational cost as dense meshes are required when dealing with non-planar fractures, or when the distances between fractures are smaller than the seismic wave length, impede its practical implementation.

In spite of dramatic development of computer science and parallel computing technology, FD methods still suffer from severe limitations regarding its huge computer memory cost and computation time. The Fourier pseudo spectral method (PSM)(Kosloff et al., 1984), as an attractive alternative method that uses an accurate differentiation scheme applying the fast Fourier transform (FFT) for calculating the spatial derivatives and uses finite

difference to calculate the time derivatives in hyperbola equations, can achieve the same accuracy as the FDM does with less grid points and hence requires less computer memory and computation time (Fornberg, 1987; Daudt et al., 1989).

Unfortunately,the periodicity condition implied by the discrete Fourier transform causes the periodically extended wavefield on either side of the computational domain to propagate in from the sides, which in turn, results in numerical contamination of waves. This phenomenon is called wraparound. To avoid this problem, Fornberg (1996) suggested to use the Chebyshev pseudo spectral method, which inevitably increases the grid density requirement to π nodes per minimum wavelength. Alternatively, absorbing boundaries (Cerjan et al., 1985), or perfectly matched layers (Collino and Tsogka, 2001) can also be used to damp the wraparound phases through a gradual reduction of the wavefield amplitude in the vicinity of the grid boundary. Liu (1998) combines the conventional Fourier pseudo spectral method with PML to effectively eliminate the wraparound effect. Furumura and Takenaka (1995) pointed out improper selection of absorption parameters can result in reflected waves of relatively large amplitude. He proposed an antiperidoic extension technique based on a simple modification of the wavefield to mitigate the wraparound, however, this method does not completely eliminate wraparound.

Another problem suffering PSM is the non-causal ringing artifacts (Gibbs phenomenon), particularly in the presence of large abrupt changes in the medium.This occurs because the Fourier transform is a global rather than a local operator: each wavenumber contributes to all space. A smooth technique is recommended by Pan and Wang (2000) to alleviate the problem caused by the discontinuities, and a similar technique is also used in Mast et al. (2001) and Tabei et al. (2002), but we note that the physical nature of the interfaces at the media discontinuities is changed by such a smooth process. Alternatively, a variable grid density pseudospectral method (Liu, 1999; Liu et al., 2000), has been proposed in which higher resolution is achieved across the interfaces of media discontinuities. However, the efficiency and the accuracy of the pseudospectral method will degrade due to the interpolation processes needed by the use of the nonuniform fast Fourier transform (NUFFT) algorithm. A rather simplified and efficient technique of using a mapping method to obtain spatial derivatives appeared in (Bayliss and Turkel, 1992; Gao et al., 2004) established a general procedure to construct mapping curves. A drawback of the procedure is found in the choice of initial grid points, although some rules in deciding the positions of grid points were proposed. A good solution was introduced by Witte et al. (1987), which involves pseudo-spectral calculation on a staggered grid to overcome the Nyquist error problem (Özdenvar and McMechan, 1996). Bale (2002) applied a staggering scheme for 3D pseudospectral modelling in fully anisotropic media, which is based on decomposing the anisotropy into orthorhombic and non-orthorhombic stiffnesses. Yet, the ringing artifacts were not completely mitigated.

Besides the wraparound and Gibbs phenomenon, the classical finite difference schemes to calculate the time derivatives are inevitably subjected to numerical dispersion. Alternatively, the rapid expansion method proposed by Kosloff et al. (1989) can be used to obtain a more accurate time integration for the second-order wave equation. Similarly to

TAL-EZER et al. (1987), Bessel functions and modified Chebyshev polynomials are incorporated in the method to expand the involved cosine operator so that it is highly accurate and numerically stable with large time steps. However, most of them are constructed for the second-order acoustic wave equation, which impedes direct use of PML boundary conditions. Long et al. (2013) proposed a temporal fourth-order scheme for solving the 2-D first-order acoustic wave equations with perfectly matched layers in time domain.

In this paper, we extend this temporal fourth-order scheme proposed by Long et al. (2013) to 3D SH-wavefield simulation in heterogeneous VTI media. The Hybird-PML (Li et al., 2016) is combined with PSTD method to eliminate wraparound effect. The PSM based on staggered-grid schemes is applied to spatial derivatives to eliminate the Gibbs phenomenon. To make a comparison, this paper also proposed SH-wavefield simulation based on second order PSTD with a sponge absorbing boundary condition (Israeli and Orszag, 1981).

FIRST-ORDER SH WAVE EQUATIONS IN VTI MEDIA

In VTI media, the stress-strain relationship in matrix form can be described as

$$c_{VTI} = \begin{bmatrix} c_{11} & c_{11}-2c_{66} & c_{13} & 0 & 0 & 0 \\ c_{11}-2c_{66} & c_{11} & c_{13} & 0 & 0 & 0 \\ c_{13} & c_{13} & c_{33} & 0 & 0 & 0 \\ 0 & 0 & 0 & c_{44} & 0 & 0 \\ 0 & 0 & 0 & 0 & c_{44} & 0 \\ 0 & 0 & 0 & 0 & 0 & c_{66} \end{bmatrix}. \tag{1}$$

And the stress-displacement relationship is

$$\varepsilon_{ij} = \frac{\mathbf{u}_{i,j} + \mathbf{u}_{j,i}}{2}. \tag{2}$$

Substitute equation(2) into equation(1), according to the equations of motion,

$$\begin{aligned} \rho\frac{\partial^2 u_x}{\partial t^2} &= \frac{\partial \sigma_{xx}}{\partial x} + \frac{\partial \sigma_{xy}}{\partial y} + \frac{\partial \sigma_{xz}}{\partial z} \\ \rho\frac{\partial^2 u_y}{\partial t^2} &= \frac{\partial \sigma_{xy}}{\partial x} + \frac{\partial \sigma_{yy}}{\partial y} + \frac{\partial \sigma_{yz}}{\partial z} \\ \rho\frac{\partial^2 u_z}{\partial t^2} &= \frac{\partial \sigma_{xz}}{\partial x} + \frac{\partial \sigma_{yz}}{\partial y} + \frac{\partial \sigma_{zz}}{\partial z} \end{aligned} . \tag{3}$$

We get the wave equations in VTI media,

$$\begin{aligned} &c_{11}\frac{\partial \nabla_2\cdot\mathbf{u_2}}{\partial x} + c_{13}\frac{\partial^2 u_z}{\partial x \partial z} + c_{66}\frac{\partial}{\partial y}\left(\frac{\partial u_x}{\partial y} - \frac{\partial u_y}{\partial x}\right) + c_{44}\frac{\partial}{\partial z}\left(\frac{\partial u_x}{\partial z} - \frac{\partial u_z}{\partial x}\right) + \rho\omega^2 u_x = 0 \\ &c_{11}\frac{\partial \nabla_2\cdot\mathbf{u_2}}{\partial y} + c_{13}\frac{\partial^2 u_z}{\partial y \partial z} + c_{66}\frac{\partial}{\partial x}\left(\frac{\partial u_y}{\partial x} - \frac{\partial u_x}{\partial y}\right) + c_{44}\frac{\partial}{\partial z}\left(\frac{\partial u_y}{\partial z} - \frac{\partial u_z}{\partial y}\right) + \rho\omega^2 u_y = 0 \\ &(c_{13}+c_{44})\frac{\partial \nabla_2\cdot\mathbf{u_2}}{\partial z} + c_{33}\frac{\partial^2 u_z}{\partial z^2} + c_{44}\nabla_2^2 u_z + \rho\omega^2 u_z = 0 \end{aligned} , \tag{4}$$

where, ∇_2 is an operator in xy plane and satisfies $\nabla_2 = \hat{\mathbf{x}}\frac{\partial}{\partial x} + \hat{\mathbf{y}}\frac{\partial}{\partial y}$; $\mathbf{u}_2$ is the projection of $\mathbf{u}$ in xy plane and has $\mathbf{u}_2 = \hat{\mathbf{x}}u_x + \hat{\mathbf{y}}u_y$. The displacement of elastic wave equation $\mathbf{u}$ can be described as

$$\mathbf{u} = \nabla\varphi + \nabla \times (\chi\hat{\mathbf{z}}) + \nabla \times \nabla \times (\eta\hat{\mathbf{z}}), \tag{5}$$

where, φ, η and χ are the scalar displacement potentials. Extend equation (5) such that

$$\begin{aligned} u_x &= \tfrac{\partial\varphi}{\partial x} + \tfrac{\partial\chi}{\partial y} + \tfrac{\partial^2\eta}{\partial x\partial z} \\ u_y &= \tfrac{\partial\varphi}{\partial y} - \tfrac{\partial\chi}{\partial x} + \tfrac{\partial^2\eta}{\partial y\partial z} \quad . \\ u_z &= \tfrac{\partial\varphi}{\partial z} - \tfrac{\partial^2\eta}{\partial x^2} + \tfrac{\partial^2\eta}{\partial y^2} \end{aligned} \tag{6}$$

Substitute equation (6) into equation (4), we have,

$$\begin{aligned} &c_{11}\nabla_2^2\varphi + (c_{13}+2c_{44})\tfrac{\partial^2\varphi}{\partial z^2} + \rho\omega^2\varphi + \tfrac{\partial}{\partial z}\left[(c_{11}-c_{13}-c_{44})\nabla_2^2\eta + c_{44}\tfrac{\partial^2\eta}{\partial z^2} + \rho\omega^2\eta\right] = 0 \\ &\tfrac{\partial}{\partial z}\left[(c_{13}+2c_{44})\nabla_2^2\varphi + c_{33}\tfrac{\partial^2\varphi}{\partial z^2} + \rho\omega^2\varphi\right] - \nabla_2^2\left[c_{44}\nabla_2^2\eta + (c_{33}-c_{13}-c_{44})\tfrac{\partial^2\eta}{\partial z^2} + \rho\omega^2\eta\right] = 0 \cdot \\ &c_{66}\nabla_2^2\chi + c_{44}\tfrac{\partial^2\chi}{\partial z^2} + \rho\omega^2\chi = 0 \end{aligned} \tag{7}$$

The first two equations of equation (7) are the coupled equations of φ and η (P- and SV-wave respectively). The exact dispersion relation of the P and SV waves for VTI media is derived by Tsvankin (1996):

$$\frac{v^2(\theta)}{v_{po}^2} = 1 + \varepsilon\sin^2\theta - \frac{f}{2} \pm \frac{f}{2}\left[1 + \frac{2\varepsilon\sin^2\theta}{f}\right]\left[1 - \frac{2(\varepsilon-\delta)\sin^2 2\theta}{f(1+\frac{2\varepsilon\sin^2\theta}{f})^2}\right]^{1/2}, \tag{8}$$

where θ is the phase angle measured from the symmetry axis, $v(\theta)$ is the phase velocity of the coupled wave modes; ε, δ, and γ(which will be discussed later) denote the Thomsen (1986) parameters, which are defined as

$$\begin{aligned} \varepsilon &= \tfrac{c_{11}-c_{33}}{2c_{33}}; \qquad \gamma = \tfrac{c_{66}-c_{44}}{2c_{44}}; \\ \delta &= \tfrac{(c_{13}+c_{44})^2-(c_{33}-c_{44})^2}{2c_{33}(c_{33}-c_{44})} \quad . \end{aligned} \tag{9}$$

And $f = 1 - \left(\frac{v_{so}}{v_{po}}\right)^2$, where v_{po} and v_{so} denote P- and SV-wave velocities along the symmetry axis, where $v_{po} = \sqrt{c_{33}/\rho}$ and $v_{so} = \sqrt{c_{44}/\rho}$ in VTI medium. The plus and minus signs correspond to the P and SV-wave, respectively.

The last term of equation (7) is SH-wave equation in VTI medium. Let vector $\mathbf{v}$ ($\mathbf{v} = (v_x, v_y, v_z)^T$) be the particle velocity and $\mathbf{X}$ ($\mathbf{X} = (\chi_x, \chi_y, \chi_z)^T$) based on the split-field

technique (Chew and Weedon, 1994; Collino and Tsogka, 2001), the SH-wave equation can be described as the following first-order system

$$\begin{aligned}
\frac{\partial v_x}{\partial t} &= -\frac{c_{66}}{\rho}\left(\frac{\partial \chi_x}{\partial x} + \frac{\partial \chi_y}{\partial x} + \frac{\partial \chi_z}{\partial x}\right) \\
\frac{\partial v_y}{\partial t} &= -\frac{c_{66}}{\rho}\left(\frac{\partial \chi_x}{\partial y} + \frac{\partial \chi_y}{\partial y} + \frac{\partial \chi_z}{\partial y}\right) \\
\frac{\partial v_z}{\partial t} &= -\frac{c_{44}}{\rho}\left(\frac{\partial \chi_x}{\partial z} + \frac{\partial \chi_y}{\partial z} + \frac{\partial \chi_z}{\partial z}\right) \\
\frac{\partial \chi_x}{\partial t} &= -\frac{\partial v_x}{\partial x} \\
\frac{\partial \chi_y}{\partial t} &= -\frac{\partial v_y}{\partial y} \\
\frac{\partial \chi_z}{\partial t} &= -\frac{\partial v_z}{\partial z}
\end{aligned} . \tag{10}$$

The above first-order system can then be expressed as a matrix form

$$\begin{aligned}
\frac{\partial \mathbf{v}}{\partial t} &= \mathbf{A}\mathbf{X} \\
\frac{\partial \mathbf{X}}{\partial t} &= \mathbf{B}\mathbf{v}
\end{aligned} . \tag{11}$$

where **A** and **B** are expressed as

$$\mathbf{A} = \begin{bmatrix} -\frac{c_{66}}{\rho}\frac{\partial}{\partial x} & -\frac{c_{66}}{\rho}\frac{\partial}{\partial x} & -\frac{c_{66}}{\rho}\frac{\partial}{\partial x} \\ -\frac{c_{66}}{\rho}\frac{\partial}{\partial y} & -\frac{c_{66}}{\rho}\frac{\partial}{\partial y} & -\frac{c_{66}}{\rho}\frac{\partial}{\partial y} \\ -\frac{c_{44}}{\rho}\frac{\partial}{\partial z} & -\frac{c_{44}}{\rho}\frac{\partial}{\partial z} & -\frac{c_{44}}{\rho}\frac{\partial}{\partial z} \end{bmatrix}, \tag{12}$$

and,

$$\mathbf{B} = \begin{bmatrix} -\frac{\partial}{\partial x} & 0 & 0 \\ 0 & -\frac{\partial}{\partial y} & 0 \\ 0 & 0 & -\frac{\partial}{\partial z} \end{bmatrix}. \tag{13}$$

STAGGERED-GRID FOURIER PSEUDOSPECTORAL DERIVATIVES

According to Witte and Richards (1990), the first-order Fourier derivative of a function u(x) can be discretized over a finite grid of N points by

$$\mathcal{D}_x u(x_i) = \mathcal{DFT}^{-1}\left[-jk_x \mathcal{DFT}\left(u(x_i)\right)\right]. \tag{14}$$

where $j = \sqrt{-1}$, and $x_i = i \triangle x, i = 1, ..., N-1$, with $\triangle x$ being the sampling interval. k_x, given by $k_x = 2n\pi/(N \triangle x)$ is the discrete wavenumber in x direction. For an even N, n should be chosen as $-N/2 \leq n \leq N/2$, where $n = -N/2$ corresponds to the

Nyquist wavenumber. For an odd N, we can choose $-N/2 < n < N/2$, and in this case the Nyquist wavenumber does not correspond to one of the grid points. The abbreviations $\mathcal{DFT}$and $\mathcal{DFT}^{-1}$ corresponding to the forward and inverse discrete Fourier transforms, respectively. In homogeneous medium, the conventional Fourier derivative of equation (14) can provide satisfactory results. However, as Özdenvar and McMechan (1996) points out that the ringing effects or more specifically, the Gibbs phenomenon will emerge if the waveform propagates in heterogeneous media. Compared with the conventional Fourier transforms, the staggered-grid Fourier pseudospectral differentiation has an advantage of reducing ripple errors caused by phase jumps at the Nyquist wavenumber. The staggered-grid version of the first-order derivative of u(x) can be described in terms of the half-grid-spacing phase-shift of the standard Fourier derivative as

$$\mathcal{D}_x^{\pm} u(x_{i\pm\frac{1}{2}}) = \mathcal{DFT}^{-1}\left[-jk_x exp\left(\frac{\mp jk_x \triangle x}{2}\right)\mathcal{DFT}\left(u(x_i)\right)\right]. \tag{15}$$

in which $'\pm'$ denotes the forward and backward differentiations. Similarly,the high-order derivatives at mid-points $x_{i\pm\frac{1}{2}}$ can be described as

$$\mathcal{D}_{x^m}^{\pm} u(x_{i\pm\frac{1}{2}}) = \mathcal{DFT}^{-1}\left[(-jk_x)^m exp\left(\frac{\mp jk_x \triangle x}{2}\right)\mathcal{DFT}\left(u(x_i)\right)\right], \tag{16}$$

for an odd m. When m is even, the m^th derivatives at point x_i should be

$$\mathcal{D}_{x^m} u(x_i) = \mathcal{DFT}^{-1}\left[(-jk_x)^m \mathcal{DFT}\left(u(x_i)\right)\right]. \tag{17}$$

Equation (11) can be expanded as

$$\begin{aligned} &\mathbf{v}\left(t+\tfrac{1}{2}\triangle t\right) - \mathbf{v}\left(t-\tfrac{1}{2}\triangle t\right) \approx (\triangle t\mathbf{A} + \tfrac{1}{24}\triangle t^3\mathbf{ABA})\mathbf{X}(t) \\ &\mathbf{X}(t+\triangle t) - \mathbf{X}(t) \approx \left(\triangle t\mathbf{B} + \tfrac{1}{24}\triangle t^3\mathbf{BAB}\right)\mathbf{v}(t+\tfrac{1}{2}\triangle t) \end{aligned} . \tag{18}$$

The spatial derivatives of above equations can be approximated by the Fourier derivatives as

$$
\begin{aligned}
v_x^{t+\frac{1}{2}\triangle t} &= v_x^{t-\frac{1}{2}\triangle t} - \left[\triangle t\frac{c_{66}}{\rho}\mathcal{D}_x^+ + \frac{1}{24}\triangle t^3\frac{c_{66}^2}{\rho^2}\left[\mathcal{D}_{x^3}^+ + \mathcal{D}_x^+\mathcal{D}_{y^2} + \mathcal{D}_x^+\mathcal{D}_{z^2}\right]\right](\chi_x+\chi_y+\chi_z)\\
v_y^{t+\frac{1}{2}\triangle t} &= v_y^{t-\frac{1}{2}\triangle t} - \left[\triangle t\frac{c_{66}}{\rho}\mathcal{D}_y^+ + \frac{1}{24}\triangle t^3\frac{c_{66}^2}{\rho^2}\left[\mathcal{D}_{y^3}^+ + \mathcal{D}_y^+\mathcal{D}_{x^2} + \mathcal{D}_y^+\mathcal{D}_{z^2}\right]\right](\chi_x+\chi_y+\chi_z)\\
v_z^{t+\frac{1}{2}\triangle t} &= v_z^{t-\frac{1}{2}\triangle t} - \left[\triangle t\frac{c_{44}}{\rho}\mathcal{D}_z^+ + \frac{1}{24}\triangle t^3\frac{c_{44}^2}{\rho^2}\left[\mathcal{D}_{z^3}^+ + \mathcal{D}_z^+\mathcal{D}_{x^2} + \mathcal{D}_z^+\mathcal{D}_{y^2}\right]\right](\chi_x+\chi_y+\chi_z)\\
\chi_x^{t+\triangle t} &= \chi_x^t - \left[\left(\triangle t\mathcal{D}_x^- + \frac{c_{66}}{\rho}\frac{1}{24}\triangle t^3\mathcal{D}_{x^3}^-\right) + \frac{c_{66}}{\rho}\frac{1}{24}\triangle t^3\mathcal{D}_{x^2}\mathcal{D}_y^- + \frac{c_{66}}{\rho}\frac{1}{24}\triangle t^3\mathcal{D}_{x^2}\mathcal{D}_z^-\right]v_x^{t+\frac{1}{2}\triangle t}\\
\chi_y^{t+\triangle t} &= \chi_y^t - \left[\left(\triangle t\mathcal{D}_y^- + \frac{c_{66}}{\rho}\frac{1}{24}\triangle t^3\mathcal{D}_{y^3}^-\right) + \frac{c_{66}}{\rho}\frac{1}{24}\triangle t^3\mathcal{D}_{y^2}\mathcal{D}_x^- + \frac{c_{66}}{\rho}\frac{1}{24}\triangle t^3\mathcal{D}_{y^2}\mathcal{D}_z^-\right]v_y^{t+\frac{1}{2}\triangle t}\\
\chi_z^{t+\triangle t} &= \chi_z^t - \left[\left(\triangle t\mathcal{D}_z^- + \frac{c_{44}}{\rho}\frac{1}{24}\triangle t^3\mathcal{D}_{z^3}^-\right) + \frac{c_{44}}{\rho}\frac{1}{24}\triangle t^3\mathcal{D}_{z^2}\mathcal{D}_x^+\frac{c_{44}}{\rho}\frac{1}{24}\triangle t^3\mathcal{D}_{z^2}\mathcal{D}_y^-\right]v_z^{t+\frac{1}{2}\triangle t}
\end{aligned}
\tag{19}
$$

where χ_x, χ_y and χ_z are components of scalar displacement potential χ with respect to different directions and $\chi = \chi_x + \chi_y + \chi_z$.

For the stability and dispersion relation of the above equations, by summing up the split displacement potentials we can get

$$
\begin{aligned}
\chi(t+\triangle t) = \chi(t) &- \left[\left(\triangle t\frac{\partial}{\partial x} + \frac{1}{24}\triangle t^3\frac{c_{66}}{\rho}\left(\frac{\partial^3}{\partial x^3} + \frac{\partial^2}{\partial x^2}\frac{\partial}{\partial y} + \frac{\partial^2}{\partial x^2}\frac{\partial}{\partial z}\right)\right)v_x\left(t+\frac{1}{2}\triangle t\right)\right]\\
&- \left[\left(\triangle t\frac{\partial}{\partial y} + \frac{1}{24}\triangle t^3\frac{c_{66}}{\rho}\left(\frac{\partial^3}{\partial y^3} + \frac{\partial^2}{\partial y^2}\frac{\partial}{\partial x} + \frac{\partial^2}{\partial y^2}\frac{\partial}{\partial z}\right)\right)v_y\left(t+\frac{1}{2}\triangle t\right)\right].\\
&- \left[\left(\triangle t\frac{\partial}{\partial z} + \frac{1}{24}\triangle t^3\frac{c_{44}}{\rho}\left(\frac{\partial^3}{\partial z^3} + \frac{\partial^2}{\partial z^2}\frac{\partial}{\partial x} + \frac{\partial^2}{\partial z^2}\frac{\partial}{\partial y}\right)\right)v_z\left(t+\frac{1}{2}\triangle t\right)\right]
\end{aligned}
\tag{20}
$$

with $v_x\left(t+\frac{1}{2}\triangle t\right)$,$v_y\left(t+\frac{1}{2}\triangle t\right)$, $v_z\left(t+\frac{1}{2}\triangle t\right)$ expressed as

$$
\begin{aligned}
v_x(t+\tfrac{1}{2}\triangle t) &= v_x(t-\tfrac{1}{2}\triangle t) - \left[\triangle t\frac{c_{66}}{\rho}\frac{\partial}{\partial x} + \frac{1}{24}\triangle t^3\frac{c_{66}^2}{\rho^2}\left[\frac{\partial^3}{\partial x^3} + \frac{\partial}{\partial x}\frac{\partial^2}{\partial y^2} + \frac{\partial}{\partial x}\frac{\partial^2}{\partial z^2}\right]\right]\chi \\
v_y(t+\tfrac{1}{2}\triangle t) &= v_y(t-\tfrac{1}{2}\triangle t) - \left[\triangle t\frac{c_{66}}{\rho}\frac{\partial}{\partial y} + \frac{1}{24}\triangle t^3\frac{c_{66}^2}{\rho^2}\left[\frac{\partial^3}{\partial y^3} + \frac{\partial}{\partial y}\frac{\partial^2}{\partial x^2} + \frac{\partial}{\partial y}\frac{\partial^2}{\partial z^2}\right]\right]\chi \\
v_z(t+\tfrac{1}{2}\triangle t) &= v_z(t-\tfrac{1}{2}\triangle t) - \left[\triangle t\frac{c_{44}}{\rho}\frac{\partial}{\partial z} + \frac{1}{24}\triangle t^3\frac{c_{44}^2}{\rho^2}\left[\frac{\partial^3}{\partial z^3} + \frac{\partial}{\partial z}\frac{\partial^2}{\partial y^2} + \frac{\partial}{\partial z}\frac{\partial^2}{\partial x^2}\right]\right]\chi
\end{aligned}
\tag{21}
$$

By eliminating the velocity components in equation (20), the scalar displacement potential equation with temporal fourth-order accuracy can be expressed as

$$
\chi(t+\triangle t) - 2\chi(t) + \chi(t-\triangle t) = \left(r_1 s_1 + r_2 s_2 + r_3 s_3\right)\chi(t) \tag{22}
$$

where, r_1, r_2, r_3 and s_1, s_2, s_3 are expressed as

$$
\begin{aligned}
r_1 &= \triangle t\frac{\partial}{\partial x} + \frac{1}{24}\triangle t^3\frac{c_{66}}{\rho}\left(\frac{\partial^3}{\partial x^3} + \frac{\partial^2}{\partial x^2}\frac{\partial}{\partial y} + \frac{\partial^2}{\partial x^2}\frac{\partial}{\partial z}\right) \\
r_2 &= \triangle t\frac{\partial}{\partial y} + \frac{1}{24}\triangle t^3\frac{c_{66}}{\rho}\left(\frac{\partial^3}{\partial y^3} + \frac{\partial^2}{\partial y^2}\frac{\partial}{\partial x} + \frac{\partial^2}{\partial y^2}\frac{\partial}{\partial z}\right) \\
r_3 &= \triangle t\frac{\partial}{\partial z} + \frac{1}{24}\triangle t^3\frac{c_{44}}{\rho}\left(\frac{\partial^3}{\partial z^3} + \frac{\partial^2}{\partial z^2}\frac{\partial}{\partial x} + \frac{\partial^2}{\partial z^2}\frac{\partial}{\partial y}\right) \\
s_1 &= \triangle t\frac{c_{66}}{\rho}\frac{\partial}{\partial x} + \frac{1}{24}\triangle t^3\frac{c_{66}^2}{\rho^2}\left[\frac{\partial^3}{\partial x^3} + \frac{\partial}{\partial x}\frac{\partial^2}{\partial y^2} + \frac{\partial}{\partial x}\frac{\partial^2}{\partial z^2}\right] \\
s_2 &= \triangle t\frac{c_{66}}{\rho}\frac{\partial}{\partial y} + \frac{1}{24}\triangle t^3\frac{c_{66}^2}{\rho^2}\left[\frac{\partial^3}{\partial y^3} + \frac{\partial}{\partial y}\frac{\partial^2}{\partial x^2} + \frac{\partial}{\partial y}\frac{\partial^2}{\partial z^2}\right] \\
s_3 &= \triangle t\frac{c_{44}}{\rho}\frac{\partial}{\partial z} + \frac{1}{24}\triangle t^3\frac{c_{44}^2}{\rho^2}\left[\frac{\partial^3}{\partial z^3} + \frac{\partial}{\partial z}\frac{\partial^2}{\partial y^2} + \frac{\partial}{\partial z}\frac{\partial^2}{\partial x^2}\right]
\end{aligned}
\tag{23}
$$

Based on th plan wave solution, the dispersion relation of equation (22) is,

$$
-4sin^2\left(\frac{\omega\triangle t}{2}\right) = R_1 S_1 + R_2 S_2 + R_3 S_3. \tag{24}
$$

with r_1, r_2, r_3 and s_1, s_2, s_3 in k-space as

$$\begin{aligned} R_1 &= ik_x\triangle t\left(1-\tfrac{1}{24}\triangle t^2k^2\right) \\ R_2 &= ik_y\triangle t\left(1-\tfrac{1}{24}\triangle t^2k^2\right) \\ R_3 &= ik_z\triangle t\left(1-\tfrac{1}{24}\triangle t^2k^2\right) \\ S_1 &= i\triangle t\tfrac{c_{66}}{\rho}k_x(1-\tfrac{1}{24}\triangle t^2\tfrac{c_{66}}{\rho}k^2)\ , \\ S_2 &= i\triangle t\tfrac{c_{66}}{\rho}k_y(1-\tfrac{1}{24}\triangle t^2\tfrac{c_{66}}{\rho}k^2) \\ S_3 &= i\triangle t\tfrac{c_{44}}{\rho}k_z(1-\tfrac{1}{24}\triangle t^2\tfrac{c_{44}}{\rho}k^2) \end{aligned} \tag{25}$$

where, $k=\sqrt{k_x^2+k_y^2+k_z^2}$. Further manipulate equations (24) and (25), the dispersion equation can be expressed as

$$\begin{aligned} 0\le sin^2\left(\frac{\omega\triangle t}{2}\right) &= \frac{1}{4}k_r^2\triangle t^2\frac{c_{66}}{\rho}\left[1-\frac{1}{12}k^2\triangle t^2\left(1+\frac{c_{66}}{\rho}\right)+\left(\frac{1}{24}\right)^2k^4\triangle t^4\frac{c_{66}}{\rho}\right] \\ &+\frac{1}{4}k_z^2\triangle t^2\frac{c_{44}}{\rho}\left[1-\frac{1}{12}k^2\triangle t^2\left(1+\frac{c_{44}}{\rho}\right)+\left(\frac{1}{24}\right)^2k^4\triangle t^4\frac{c_{44}}{\rho}\right]\le 1 \end{aligned} \tag{26}$$

For a model with a uniform grid spacing in each direction($\Delta x=\Delta y=\Delta z$), the Nyquist wave numbers for each k-space satisfy $k_x=k_y=k_z=\frac{\pi}{\Delta x}$. Define horizontal S-wave velocity v_{sh} that satisfies $v_{so}=\sqrt{c_{66}/\rho}$ and recall the S-wave velocities along the symmetry axis $v_{sh}=\sqrt{c_{44}/\rho}$. The two S-wave velocities satisfy

$$v_{sh}^2=v_{so}^2(1+2\gamma) \tag{27}$$

According to Wang (2001, SEG), $\gamma<0.2$ in weak anisotropic media and we may safely assume that anisotropy in sedimentary rocks are weak. Based on his study, the highest γ appears in shales (γ_{max}=0.553). Let $\gamma\le 0.5$ in this work, therefore, the stability condition can be obtained by solving the inequality,

$$0\le\frac{1}{4}\frac{\pi^2}{\triangle x^2}\triangle t^2v_{so}^2\left[3-\frac{\pi^2}{\triangle x^2}\triangle t^2v_{so}^2+\frac{27}{24^2}\frac{\pi^4}{\triangle x^4}\triangle t^4v_{so}^2\right]. \tag{28}$$

Further manipulate the above equation by neglecting the third term in the bracket,

$$\triangle tv_{so}/\triangle x\le\sqrt{3}/\pi. \tag{29}$$

H-PML BOUNDARY CONDITIONS

When PSM ia applied to wavefield simulation, computational boundaries tend to produce wraparound which must be suppressed or absorbed. The perfectly matched layer (PML) approach to boundary absorption, introduced by Berenger (1994), has been proven to be very efficient. Taking the x direction as an example, a damping profile $d_x(x)$ is created, with $d_x = 0$ in the physical domain and $d_x > 0$ in the defined PML layer. The new operator $\nabla_{\tilde{x}} = [\frac{\partial}{\partial \tilde{x}}, \frac{\partial}{\partial y}, \frac{\partial}{\partial z}]$ is thus introduced, where $\frac{\partial}{\partial \tilde{x}} = \frac{1}{s_x}\frac{\partial}{\partial x}$, $s_x = 1 + \frac{d_x}{i\omega}$.

The convolutional PML (or C-PML) method (Kuzuoglu and Mittra, 1996) or the complex frequency shifted-PML (CFS-PML) method (Bérenger, 2002) introduces a frequency-dependent term which eliminates the requirement that the velocity-stress equation be split into separate terms. The C-PML scheme involves adding not only the damping profile, but two other real variables, such that:

$$s_x = \kappa_x + \frac{d_x}{\alpha_x + i\omega}. \tag{30}$$

When $\kappa_x = 1$ and $\alpha_x = 0$, the C-PML degenerates to the classic PML case.

The multiaxial perfectly matched layer (M-PML) method has been found to be stable even for media exhibiting very large degrees of anisotropy (Meza-Fajardo and Papageorgiou, 2008). In an M-PML application, in contrast to equation (30), the s_x term is

$$s_x = \kappa_x + \frac{d_x + m_{x/y}d_y + m_{x/z}d_z}{i\omega}, \tag{31}$$

where $m_{x/y}d_y$ and $m_{x/z}$ are weighting factors.

To maximize both accuracy and stability we construct a hybrid PML (H-PML) method, that combines the advantages of both the C-PML and the M-PML through the optimization of the damping profile. Because the C-PML and M-PML are independent of one another, the two can be straightforwardly hybridized by introducing

$$s_x = \kappa_x + \frac{d_x + m_{x/y}d_y + m_{x/z}d_z}{\alpha_x + i\omega}. \tag{32}$$

Therefore the new differential operator in x direction can thus be expressed as

$$\partial_{\tilde{x}} = \bar{s}_x(t) * \partial_x. \tag{33}$$

where $\bar{s}_x(t)$ is the inverse Fourier transform of $1/s_x$ and $*$ denotes convolution. According to (Roden and Gedney, 2000; Komatitsch and Martin, 2007),

$$\bar{s}_x(t) = \frac{\delta t}{\kappa_x} - \frac{d_x}{\kappa_x^2} e^{-(d_x/\kappa_x + \alpha_x)t} H(t) = \frac{\delta t}{\kappa_x} + \zeta_x(t). \tag{34}$$

The convolution in (33) now becomes

$$\partial_{\tilde{x}} = \frac{1}{\kappa_x}\partial_x + \zeta_x(t) * \partial_x. \tag{35}$$

Komatitsch and Martin (2007) replace the above equation by

$$\partial_{\tilde{x}} = \frac{1}{\kappa_x}\partial_x + \psi_x. \tag{36}$$

where ψ_x is the memory variable updated at each time step n according to

$$\psi_x^n = b_x\psi_x^{n-1} + c_x(\partial_x)^{n-1/2}, \tag{37}$$

in which

$$\begin{aligned} b_x &= e^{-\left(\left(d_x+m_{x/y}d_y+m_{x/z}d_z\right)/\kappa_x+\alpha_x\right)\triangle t} \\ c_x &= \frac{\left(d_x+m_{x/y}d_y+m_{x/z}d_z\right)}{\kappa_x\left(\left(d_x+m_{x/y}d_y+m_{x/z}d_z\right)+\kappa_x\alpha_x\right)}\left(b_x-1\right) \end{aligned}. \tag{38}$$

Therefore, the coefficient matrix in (12) and (13) are expressed as

$$\mathbf{A} = \begin{bmatrix} -\frac{c_{66}}{\rho} & -\frac{c_{66}}{\rho} & -\frac{c_{66}}{\rho} \\ -\frac{c_{66}}{\rho} & -\frac{c_{66}}{\rho} & -\frac{c_{66}}{\rho} \\ -\frac{c_{44}}{\rho} & -\frac{c_{44}}{\rho} & -\frac{c_{44}}{\rho} \end{bmatrix} \begin{bmatrix} \frac{1}{\kappa_x}\partial_x + \psi_x \\ \frac{1}{\kappa_y}\partial_y + \psi_y \\ \frac{1}{\kappa_z}\partial_z + \psi_z \end{bmatrix}, \tag{39}$$

and,

$$\mathbf{B} = \begin{bmatrix} \left(\frac{1}{\kappa_x}\partial_x + \psi_x\right) & 0 & 0 \\ 0 & -\left(\frac{1}{\kappa_y}\partial_y + \psi_y\right) & 0 \\ 0 & 0 & \left(\frac{1}{\kappa_z}\partial_z + \psi_z\right) \end{bmatrix}. \tag{40}$$

For the above equations, if the elastic parameters and the density do not depend on space (e.g. the medium is homogeneous), they can be directly calculated in each Fourier derivative without losing accuracies. However, when these parameters vary in heterogeneous media (e.g. in layered media), they have to be calculated in the space domain, to avoid the Gibbs phenomenon.

NUMERICAL EXPERIMENTS

Bilayered medium model

In this section, a numerical example of two layer heterogeneous media will be presented to verify the accuracy of the new scheme. The computational grid is $191 \times 241 \times 291$ including a H-PML layer of 20 grids outside each computational boundary, with the grid spacings $\triangle x = \triangle y = \triangle z = 0.04m$. A dipole source composed of two Ricker wavelets with central frequency $f_0 = 4000Hz$ is used for the simulation. Based on the stability

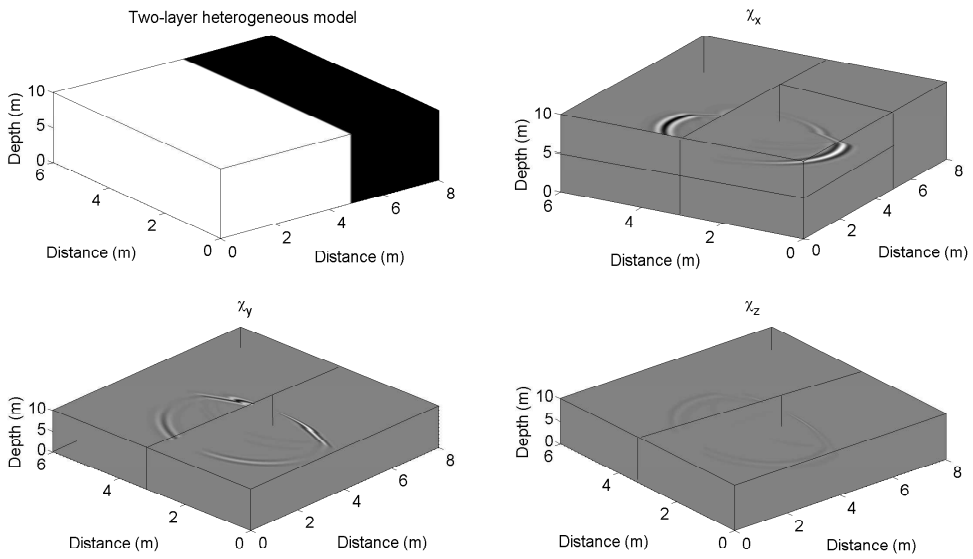

FIG. 1: 3D layered model and displacement component snapshots for each direction

condition in (29), we choose the time step to be $\triangle t = 1 \times 10^{-5} s$. Figure (1) (a) shows the two-layer model.

The left layer of the model is a VTI medium, in which the elastic constants matrix is

$$c = \begin{bmatrix} 26.37 & 10.57 & 9.57 & 0 & 0 & 0 \\ 10.57 & 26.37 & 9.57 & 0 & 0 & 0 \\ 9.57 & 9.57 & 36.73 & 0 & 0 & 0 \\ 0 & 0 & 0 & 12.45 & 0 & 0 \\ 0 & 0 & 0 & 0 & 12.45 & 0 \\ 0 & 0 & 0 & 0 & 0 & 8.08 \end{bmatrix} \times 10^9. \tag{41}$$

The right layer of this model is an isotropic medium, whose P- and S- wave velocities are 2300 m/s and 1000 m/s. The density of each layer is $2500 kg/m^3$ and $2000 kg/m^3$, respectively. The other three figures in Figure (1) show the displacement component snapshots for each direction. The dipole source is directed in X direction and the SH wave is polarized in the horizontal plane, the amplitude is strongest in x direction.

Figure (2) shows the corresponding snapshots for SH propagation in x-y lateral and x-z vertical sections. To make a comparison, Figure (3) shows snapshots for SH propagation in x-y lateral and x-z vertical sections using second order PSTD method with a sponge absorbing boundary. When time=0.001 (s), both snapshots in x-y and x-z plane obtained by the new developed method show clear waveforms without any wraparound at computational boundaries; snapshots developed by the second order PSTD method when time=0.001 (s) illustrated in (3) suffer severely from the wraparound. When time=0.003 (s), the snapshots obtained by second order PSTD method are also contaminated by the boundary reflections.

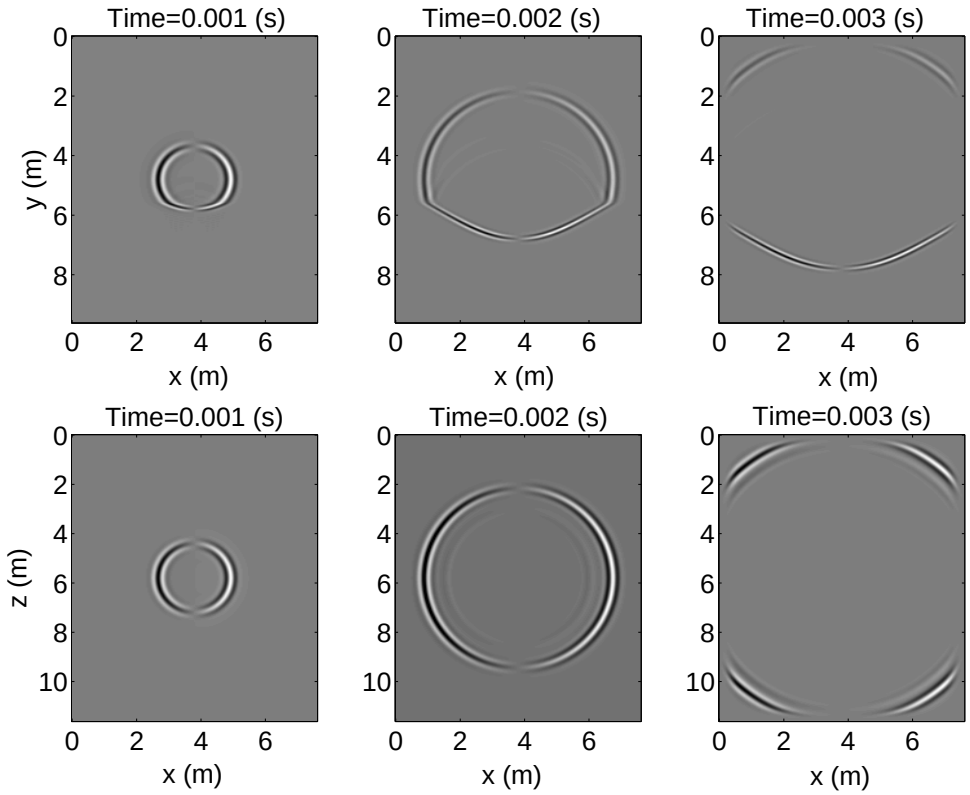

FIG. 2: Snapshots for SH propagation in x-y lateral and x-z vertical sections using PSTD staggered-grid method with H-PML

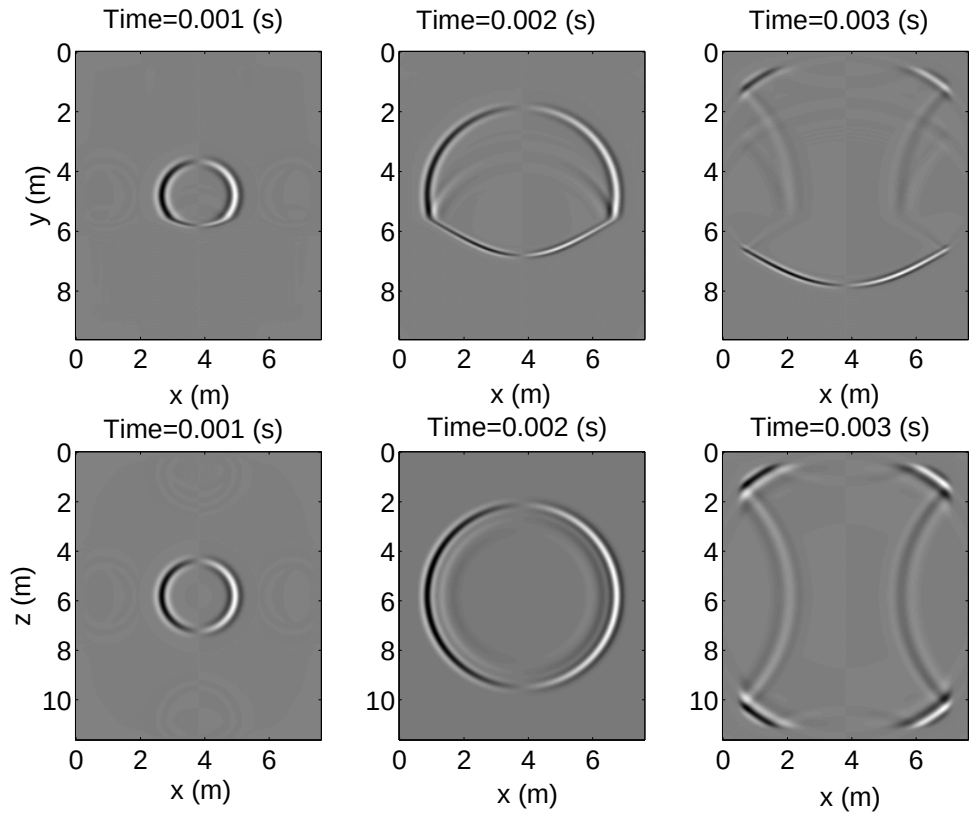

FIG. 3: Snapshots for SH propagation in x-y lateral and x-z vertical sections using second order PSTD method with a sponge absorbing boundary

When time=0.002 (s), the Gibbs phenomenon can be detected around reflection mode when second order PSTD method is used. On the contrary, neither the wraparound effect nor the Gibbs phenomenon occurs with the increasing of recoding time when the new method is used.

Figure (5) shows the recorded waveform differences between the conventional and new proposed PSTD method from four recorded receivers (receiver A to D), whose distribution in the model is shown in Figure (4), where, the blue surface is the interface, blue and red circle denote the dipole source emitting energy towards x direction. Receiver pairs A, B and C, D are symmetrically located on each side of dipole, as a result, they have the same arrival time yet opposite amplitudes. As is shown, the Rick wavelet shape event is the direct arrival, the two methods match quite well for the direct arrivals expect some trivial differences at each side of the jump, and oscillations die down abruptly for the direct arrivals. The next event occurs at about 1.8 ms, which is the reflected wave signal from the interface, the amplitude of the reflected signals acquired by the conventional PSTD is smaller than that obtained by the staggered-grid PSTD. And the oscillations or Gibbs phenomenon keep present for quite a long period, which can be detected in the dashed squares. This in turn, leads to non-negligible errors even far from the jump. On the other

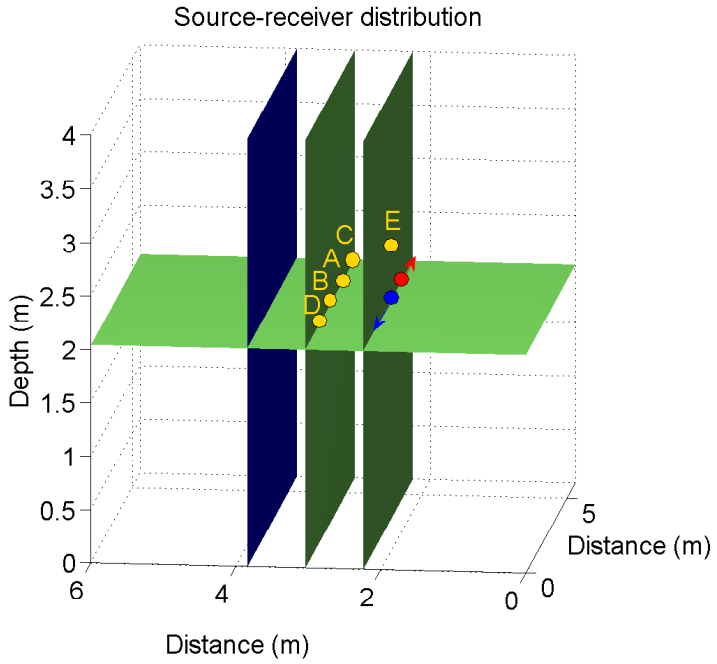

FIG. 4: Source and receiver distribution for the 2-layered model

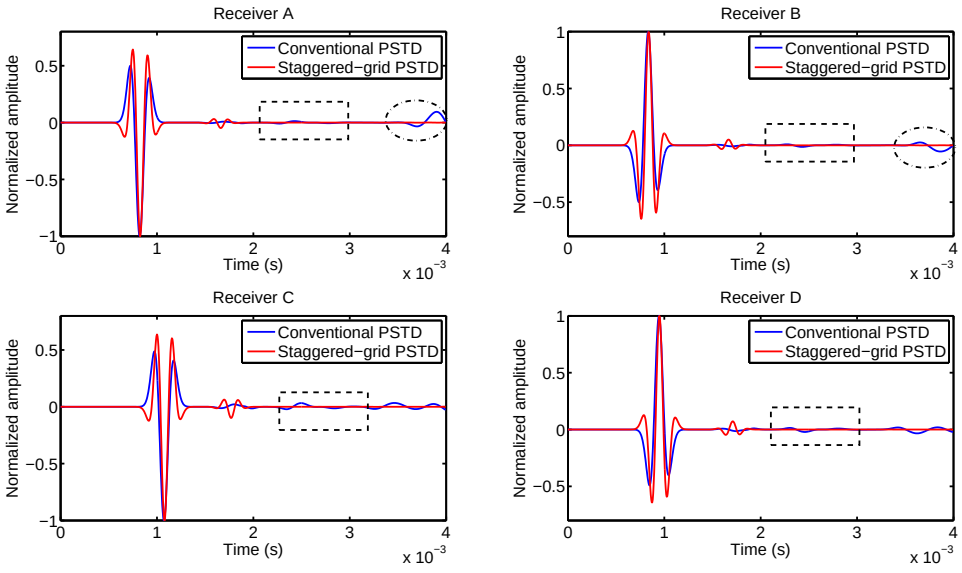

FIG. 5: Waveform comparisons between conventional and new proposed PSTD recorded by four different location

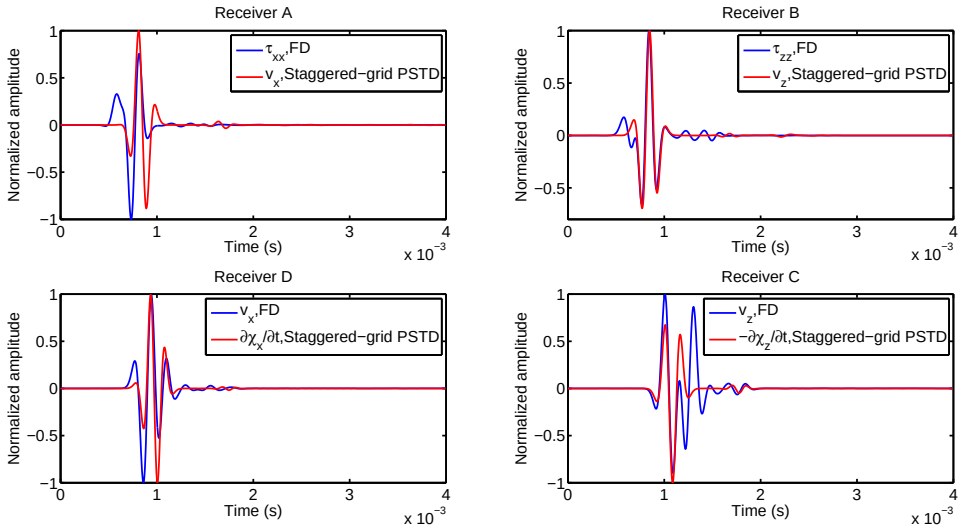

FIG. 6: Waveform comparisons between staggered-grid FD and new proposed PSTD recorded by four different location

hand, the conventional PSTD method also suffers severely from the boundary reflection artifacts, which is apparently displayed in the ecliptic areas in Figure (5).

Figure (6) shows the recorded waveform differences between the staggered-grid FD and new proposed PSTD method from four recorded receivers (receiver A to D).

According to the similarity between equation (10) and the first order velocity-stress wave equation, $\frac{\partial v_x}{\partial t}$ can be equivalently treaded as $\frac{\partial \tau_{xx}}{\partial t}$. Therefore, the comparisons between normal stress component τ_{xx} obtained by staggered grid FD and v_x calculated by our new PSTD for receiver A and B are illustrated. The peak event is the direct arrival, the two methods match quite well for the direct arrivals expect some trivial differences at side lobes. However, the oscillations for the FD method lingers out to till almost 2 ms when reflection signals arrive, which may be the reason why the reflection peak for FD can hardly be detected for receiver A and B. On the contrary, oscillations die down abruptly for the new proposed PSTD method and the reflection signals can be found at about 1.8 ms. For receiver C and D, according to equation (19), $\frac{\partial \chi_i}{\partial t}$ equals to v_i (i=x,y,z), we therefore illustrate the waveforms of v_x obtained by staggered grid FD and $\frac{\partial \chi_i}{\partial t}$ calculated by our new PSTD. The two methods match quite well for the direct arrivals for receiver D, however, the direct signal obtained by staggered FD for receiver C is followed by strong side lobes, whereas oscillations stop rapidly for the staggered-grid PSTD method. Reflection signals for both methods overlap at about 1.8 ms.

One of the advantages that should be affirmed is the displacement components as well as the velocity component are measured by the new proposed method, which can be directly used for full waveform inversion. The derivative of displacement with respect to time $\frac{\partial \chi_i}{\partial t}$ is the velocity component v_i in i direction (i=x,y,z), which can be acquired during the updating

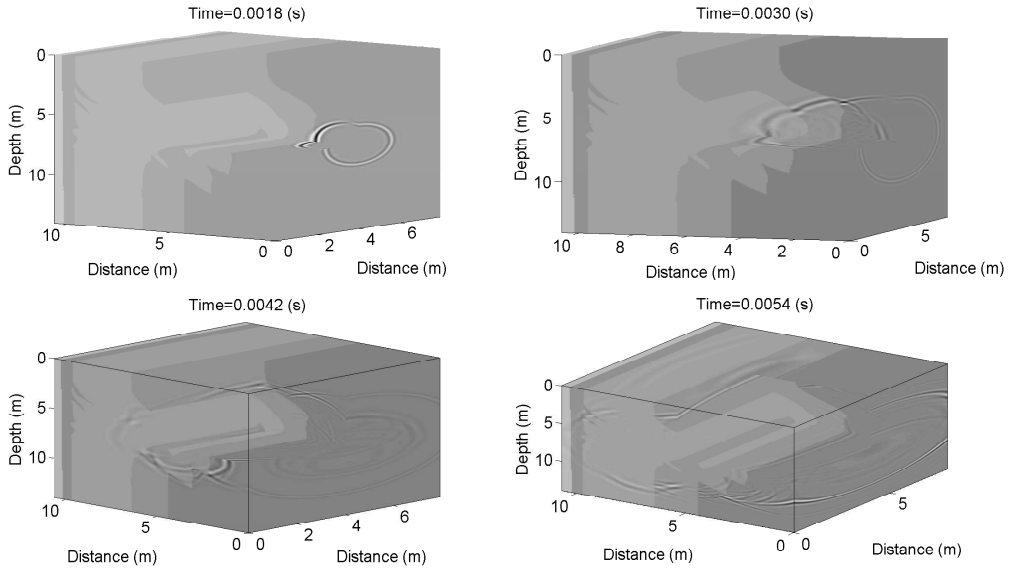

FIG. 7: Snapshots for SH propagation in thrust fault model with $\Delta t = 10\mu s$, The dipole source is located at (0.96 m, 3.84 m, 5.42 m) and (1.04 m, 3.84 m, 5.42 m)

of displacement components. Whereas, the velocity components are not available through conventional PSTD method, and the displacement components for each direction can not be directly updated through staggered-grid FD method neither. As is discussed in our other paper (Gradient calculation for anisotropic FWI), the source implementing with different components in both forward simulation and time reversing procedure plays an important role in the gradient calculation, which in turn, influences the FWI results. Based on our results, different sources are sensitive to different formation parameters.

3D thrust fault anisotropic model

In this section, a heterogeneous anisotropic model with complicated thrust faults is used to test the stability of the new scheme. The model is based on part of the thrust fault model, we duplicate the 2D thrust fault model(set as x-z plane) towards y direction into a 3D model. The first layer of this model is isotropic, with Vp- and Vs- velocities as 2400 m/s and 1280 m/s respectively. The virtical P- wave velocity of the model ranges from 2400 m/s in first layer to 6000 m/s in bottom layer. The model size is $12m \times 9.6m \times 16.8m$ and a total grid number of $200 \times 160 \times 280$. The source used in this model is a dipole x-directional source with a Ricker wavelet whose dominant frequency is 3 kHz. The space and time interval used in this model are 0.04 m and 10 μs. For the same model, the maximum space and time interval for the second order in time and forth-order in space finite difference method is 0.03 m and 4.5 μs. Figure (7) shows the wavefield propagation with different recording times. The Ricker wavelet is located at (1 m, 3.84 m, 5.42 m) and (1 m, 3.84 m, 5.42 m).

Figure (8) and (9) show the SH wavefield propagation with different recording times in

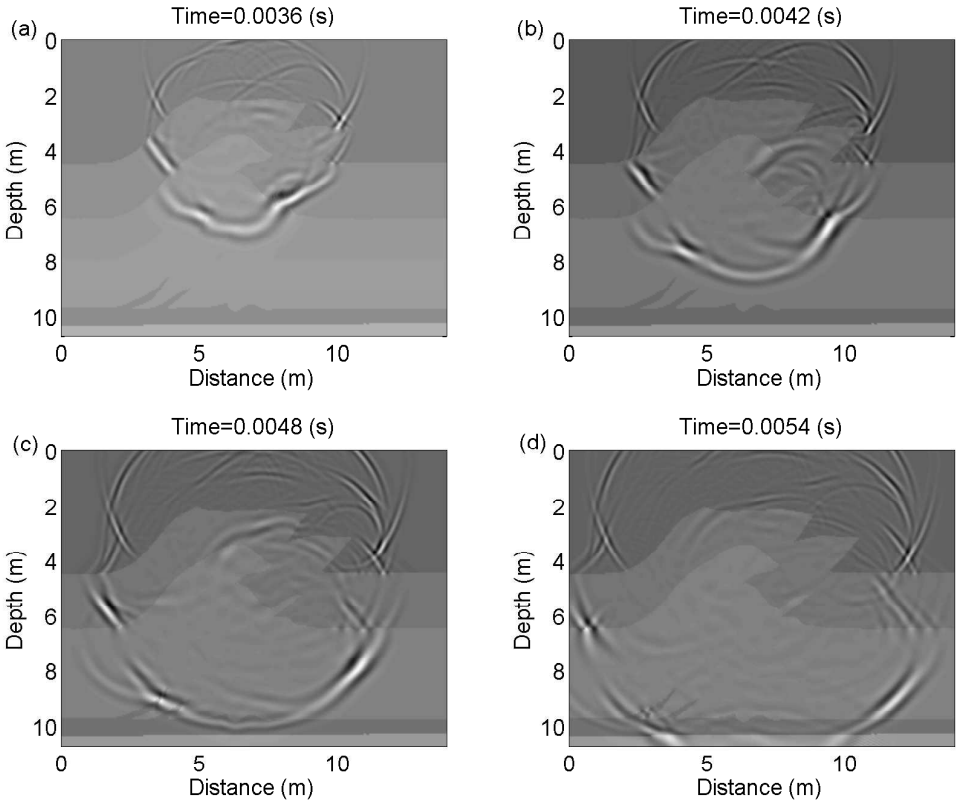

FIG. 8: Snapshots for SH propagation in thrust fault model (x-z plane)

x-z plane and x-y plane. With the increase of recording time, the SH wave travels from the isotropic media through anisotropic layered medium without any wraparound effect, and the there's also no evidence of the Gibbs phenomenon that interferes the snapshots.

CONCLUSION AND DISCUSSION

In this paper, a temporal fourth-order scheme for solving the SH- wave equations in VTI media has been proposed to solve the wraparound effect and Gibbs phenomenon due to the heterogeneity of the formation especially when large abrupt changes in the medium are present. The efficiency of new method is hindered to a certain degree because of the calculation of Fourier derivatives using high-order staggerer-grid method, compared with the conventional PSTD using second order centered-grid Fourier derivatives. Nevertheless, the H-PML can be successfully added after the SH wave equation has been reduced into a first-order equation, which in turn eliminates the wraparound effect. The numerical result for a bilayered model shows the accuracy of this scheme. The conventional second-order scheme result is also shown, which suffers from both the wraparound effect and Gibbs artifacts. Experiments for the 3D anisotropic thrust fault model have also demonstrated the efficiency and accuracy of the proposed scheme.

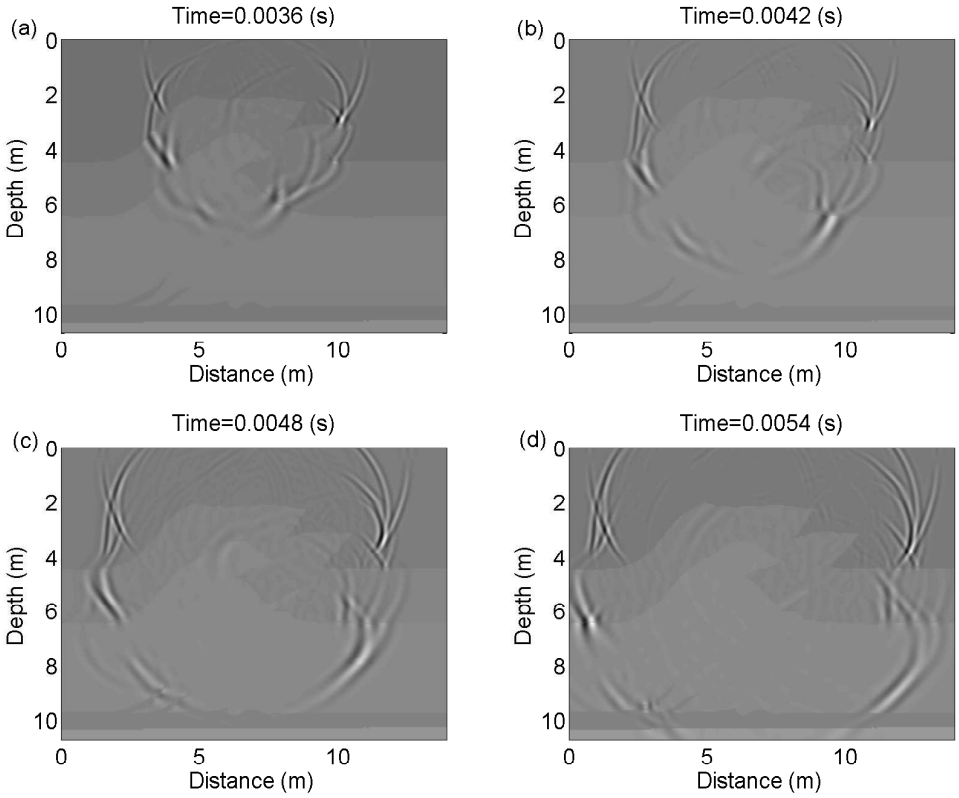

FIG. 9: Snapshots for SH propagation in thrust fault model (x-y plane)

The stability condition for this scheme is also discussed in this paper, for a specific space interval that meets the requirement for the PSTD, the maximum time step for stability is calculated. Compared with second-order in time and fourth order in space staggered grid finite difference method, larger space and time interval can be selected, thus the computational cost is greatly reduced as a result.

However, for further validation of this method, a benchmark with the analytical solution is needed. Although the computational cost can be greatly reduced compared with the FD methods, its efficiency is geared down in terms of the calculation of the first-order Fourier derivatives instead of computing the second order Fourier derivatives directly. This new scheme is inspired by previous study on the SH amplitude in borehole environment, a more detailed study on migration and full waveform inversion using this new scheme will be our further work after some benchmarks. Nevertheless, it should also be noticed that the displacement components as well as the velocity component are measured by the new proposed method, which can be directly used for full waveform inversion.

ACKNOWLEDGMENTS

This research was supported by the Consortium for Research in Elastic Wave Exploration Seismology (CREWES) and National Science and Engineering Research Council of Canada (NSERC, CRDPJ 379744-08). The first author also thanks to the supporting by SEG and CSEG scholarship.

REFERENCES

Alford, R., Kelly, K., and Boore, D. M., 1974, Accuracy of finite-difference modeling of the acoustic wave equation: Geophysics, **39**, No. 6, 834–842.

Alterman, Z., and Karal, F., 1968, Propagation of elastic waves in layered media by finite difference methods: Bulletin of the Seismological Society of America, **58**, No. 1, 367–398.

Bale, R. A., 2002, Staggered grids for 3d pseudospectral modeling in anisotropic elastic media: Calgary: CREWES Research Report.

Bayliss, A., and Turkel, E., 1992, Mappings and accuracy for chebyshev pseudo-spectral approximations: Journal of Computational Physics, **101**, No. 2, 349–359.

Berenger, J.-P., 1994, A perfectly matched layer for the absorption of electromagnetic waves: Journal of computational physics, **114**, No. 2, 185–200.

Bérenger, J.-P., 2002, Application of the cfs pml to the absorption of evanescent waves in waveguides: IEEE Microwave and Wireless Components Letters, **12**, No. 6, 218–220.

Boore, D. M., 1970a, Finite difference solutions to the equations of elastic wave-propagation, with application to love waves over dipping interfaces.: Ph.D. thesis, Massachusetts Institute of Technology.

Boore, D. M., 1970b, Love waves in nonuniform wave guides: Finite difference calculations: Journal of Geophysical Research, **75**, No. 8, 1512–1527.

Cerjan, C., Kosloff, D., Kosloff, R., and Reshef, M., 1985, A nonreflecting boundary condition for discrete acoustic and elastic wave equations: Geophysics, **50**, No. 4, 705–708.

Chew, W. C., and Weedon, W. H., 1994, A 3d perfectly matched medium from modified maxwell's equations with stretched coordinates: Microwave and optical technology letters, **7**, No. 13, 599–604.

Collino, F., and Tsogka, C., 2001, Application of the perfectly matched absorbing layer model to the linear elastodynamic problem in anisotropic heterogeneous media: Geophysics, **66**, No. 1, 294–307.

Daudt, C., Braile, L., Nowack, R., and Chiang, C., 1989, A comparison of finite-difference and fourier method calculations of synthetic seismograms: Bulletin of the Seismological Society of America, **79**, No. 4, 1210–1230.

Fornberg, B., 1987, The pseudospectral method: Comparisons with finite differences for the elastic wave equation: Geophysics, **52**, No. 4, 483–501.

Fornberg, B., 1996, A practical guide to pseudospectral methods, vol. 1 of cambridge monographs on applied and computational mathematics.

Furumura, T., and Takenaka, H., 1995, A wraparound elimination technique for the pseudospectral wave synthesis using an antiperiodic extension of the wavefield: Geophysics, **60**, No. 1, 302–307.

Gao, X., Mirotznik, M. S., Shi, S., and Prather, D. W., 2004, Applying a mapped pseudospectral time-domain method in simulating diffractive optical elements: JOSA A, **21**, No. 5, 777–785.

Igel, H., and Weber, M., 1995, Sh-wave propagation in the whole mantle using high-order finite differences: Geophysical Research Letters, **22**, No. 6, 731–734.

Israeli, M., and Orszag, S. A., 1981, Approximation of radiation boundary conditions: Journal of Computational Physics, **41**, No. 1, 115–135.

Kelly, P. H., and Iversen, S. D., 1976, Selective 60hda-induced destruction of mesolimbic dopamine neurons: abolition of psychostimulant-induced locomotor activity in rats: European journal of pharmacology, **40**, No. 1, 45–56.

Kosloff, D., Queiroz Filho, A., Tessmer, E., and Behle, A., 1989, Numerical solution of the acoustic and elastic wave equations by a new rapid expansion method: Geophysical Prospecting, **37**, No. 4, 383–394.

Kosloff, D., Reshef, M., and Loewenthal, D., 1984, Elastic wave calculations by the fourier method: Bulletin of the Seismological Society of America, **74**, No. 3, 875–891.

Kummer, B., and Behle, A., 1982, Second-order finite-difference modeling of sh-wave propagation in laterally inhomogeneous media: Bulletin of the Seismological Society of America, **72**, No. 3, 793–808.

Kuzuoglu, M., and Mittra, R., 1996, Frequency dependence of the constitutive parameters of causal perfectly matched anisotropic absorbers: Microwave and Guided Wave Letters, IEEE, **6**, No. 12, 447–449.

Li, J., Innanen, K., Lines, L., and Tao, G., 2016, Wavefield simulation of 3d borehole dipole radiation, *in* SEG Technical Program Expanded Abstracts 2016, Society of Exploration Geophysicists, 744–748.

Liu, Q. H., 1998, The pseudospectral time-domain (pstd) algorithm for acoustic waves in absorptive media: IEEE transactions on ultrasonics, ferroelectrics, and frequency control, **45**, No. 4, 1044–1055.

Liu, Q. H., 1999, Large-scale simulations of electromagnetic and acoustic measurements using the pseudospectral time-domain (pstd) algorithm: IEEE Transactions on Geoscience and Remote Sensing, **37**, No. 2, 917–926.

Liu, Q. H., Xu, X. M., Tian, B., and Zhang, Z. Q., 2000, Applications of nonuniform fast transform algorithms in numerical solutions of differential and integral equations: IEEE Transactions on geoscience and remote sensing, **38**, No. 4, 1551–1560.

Long, G., Zhao, Y., and Zou, J., 2013, A temporal fourth-order scheme for the first-order acoustic wave equations: Geophysical Journal International, **194**, No. 3, 1473–1485.

Madariaga, R., 1976, Dynamics of an expanding circular fault: Bulletin of the Seismological Society of America, **66**, No. 3, 639–666.

Mast, T. D., Souriau, L. P., Liu, D.-L., Tabei, M., Nachman, A. I., and Waag, R. C., 2001, A k-space method for large-scale models of wave propagation in tissue: IEEE transactions on ultrasonics, ferroelectrics, and frequency control, **48**, No. 2, 341–354.

Meza-Fajardo, K. C., and Papageorgiou, A. S., 2008, A nonconvolutional, split-field, perfectly matched layer for wave propagation in isotropic and anisotropic elastic media: stability analysis: Bulletin of the Seismological Society of America, **98**, No. 4, 1811–1836.

Moczo, P., 1989, Finite-difference technique for sh-waves in 2-d media using irregular gridsâĂŤapplication to the seismic response problem: Geophysical Journal International, **99**, No. 2, 321–329.

Özdenvar, T., and McMechan, G. A., 1996, Causes and reduction of numerical artefacts in pseudo-spectral wavefield extrapolation: Geophysical Journal International, **126**, No. 3, 819–828.

Pan, J., and Wang, J., 2000, Acoustical wave propagator: The Journal of the Acoustical Society of America, **108**, No. 2, 481–487.

Slawinski, R. A., and Krebes, E. S., 2002, Finite-difference modeling of sh-wave propagation in nonwelded contact media: Geophysics, **67**, No. 5, 1656–1663.

Tabei, M., Mast, T. D., and Waag, R. C., 2002, A k-space method for coupled first-order acoustic propagation equations: Journal of the Acoustical Society of America, **111**, No. 1, 53–63.

TAL-EZER, H., Kosloff, D., and Koren, Z., 1987, An accurate scheme for seismic forward modelling: Geophysical Prospecting, **35**, No. 5, 479–490.

Thomsen, L., 1986, Weak elastic anisotropy: Geophysics, **51**, No. 10, 1954–1966.

Tsvankin, I., 1996, P-wave signatures and notation for transversely isotropic media: An overview: Geophysics, **61**, No. 2, 467–483.

Virieux, J., 1984, Sh-wave propagation in heterogeneous media: Velocity-stress finite-difference method: Geophysics, **49**, No. 11, 1933–1942.

Virieux, J., 1986, P-sv wave propagation in heterogeneous media: Velocity-stress finite-difference method: Geophysics, **51**, No. 4, 889–901.

Witte, D., and Richards, P., 1990, Computational acoustics.

Witte, D., Richards, P. G. et al., 1987, Contributions to the pseudospectral method for computing synthetic seismograms, *in* 1987 SEG Annual Meeting, Society of Exploration Geophysicists.